SCIENCE CHINA
Chemistry

•ARTICLES•

https://doi.org/10.1007/s11426-023-1945-8

Rational molecular design of efficient yellow-red dendrimer TADF for solution-processed OLEDs: a combined effect of substitution position and strength of the donors

Changfeng Si, Dianming Sun*, Tomas Matulaitis, David B. Cordes,
Alexandra M. Z. Slawin & Eli Zysman-Colman*

Organic Semiconductor Centre, EaStCHEM School of Chemistry, University of St Andrews, St Andrews, KY16 9ST, UK

Received November 29, 2023; accepted January 31, 2024; published online February 21, 2024

The development of high-performance solution-processed red organic light-emitting diodes (OLEDs) remains a challenge, particularly in terms of maintaining efficiency at high luminance. Here, we designed and synthesized four novel orange-red thermally activated delayed fluorescence (TADF) dendrimers that are solution-processable: **2GCzBP**, **2DPACzBP**, **2FBP2GCz** and **2FBP2DPACz**. We systematically investigated the effect of substitution position and strength of donors on the optoelectronic properties. The reverse intersystem crossing rate constant (k_{RISC}) of the emitters having donors substituted at positions 11 and 12 of the dibenzo[*a*,*c*]phenazine (BP) is more than 10-times faster than that of compounds substituted having donors substituted at positions 3 and 6. Compound **2DPACzBP**, containing stronger donors than **2GCzBP**, exhibits a red-shifted emission and smaller singlet-triplet energy splitting, ΔE_{ST}, of 0.01 eV. The solution-processed OLED with 10 wt% **2DPACzBP** doped in mCP emitted at 640 nm and showed a maximum external quantum efficiency (EQE$_{\max}$) of 7.8%, which was effectively maintained out to a luminance of 1,000 cd m^{-2}. Such a device's performance at relevant display luminance is among the highest for solution-processed red TADF OLEDs. The efficiency of the devices was improved significantly by using 4CzIPN as an assistant dopant in a hyperfluorescence (HF) configuration, where the **2DPACzBP** HF device shows an EQE$_{\max}$ of 20.0% at λ_{EL} of 605 nm and remains high at 11.8% at a luminance of 1,000 cd m^{-2}, which makes this device one of the highest efficiency orange-to-red HF SP-OLEDs to date.

thermally activated delayed fluorescence, solution-processing, red OLEDs, dibenzo[*a*, *c*]phenazine, dendrimers

Citation: Si C, Sun D, Matulaitis T, Cordes DB, Slawin AMZ, Zysman-colman E. Rational molecular design of efficient yellow-red dendrimer TADF for solution-processed OLEDs: a combined effect of substitution position and strength of the donors. *Sci China Chem*, 2024, 67, https://doi.org/10.1007/s11426-023-1945-8

1 Introduction

Organic light-emitting diodes (OLEDs) are now commonplace in displays in mobile phones, smartwatches and televisions and have made inroads in the solid-state lighting and automotive markets [1–6]. Most OLEDs are fabricated using a vacuum deposition technology that employs a complicated, multilayered device architecture that results in high production costs. An alternative strategy would be to fabricate the OLEDs using lower-cost solution-processing techniques such as ink-jet printing, which also would provide a much simpler route to the production of large-area displays [7,8]. To achieve comparable performance metrics as vacuum-deposited devices, the key requirement for the solution-processed (SP) OLEDs is the availability of high-performance solution-processable emitter materials. Thermally activated delayed fluorescence (TADF) materials have attracted much

---

*Corresponding authors (email: eli.zysman-colman@st-andrews.ac.uk; sundianming@hotmail.com)

attention over the last decade as replacement emitter materials for noble metal-based phosphorescent complexes in OLEDs as they are less expensive and do not incorporate scarce platinoid metals yet are equally capable of harvesting up to 100% of the excitons to produce light [1,4,5]. Although vacuum-deposited OLEDs with small molecule TADF emitters have shown outstanding efficiencies in devices across the visible spectrum, these compounds tend to crystallize and thus are not ideal for solution-processed film formation. Macromolecules, such as dendrimers or polymers, on the other hand, are perfect candidates for SP-OLEDs because of their superior film-forming ability, excellent thermal and morphological stability, and high affinity for substrates [9–13]. Significant progress has been made in the development of green and blue solution-processable TADF materials, and their corresponding SP-OLEDs exhibit outstanding maximum external quantum efficiency ($\mathrm{EQE_{max}}$) of over 20% [9,10,14–18].

Despite these achievements, there is presently a dearth of examples of efficient solution-processable red TADF emitters where their photoluminescence quantum yield (Φ_{PL}) is frequently much lower than for green and blue because of the lower radiative rate constant, k_{r}, and higher non-radiative rate constant, k_{nr}, as a result of the energy gap law [19–21]. So far, there are only a few reports of relatively efficient red TADF emitters for SP-OLEDs (Figure 1a). Zhang *et al.* [22] reported an orange-red emitter **4t-BuCzTTR** by using thianthrene 5,5,10,10-tetraoxide as the acceptor, 3,6-di-*tert*-butyl-9*H*-carbazole (*t*Cz) as the donor and the resulting SP-OLEDs emitted at λ_{EL}= 592 nm and showed an $\mathrm{EQE_{max}}$ of 6.2%, which dropped to around ~4.0% at 1,000 cd m^{-2} ($\mathrm{EQE_{1000}}$). A deep red wedge-shaped organic fluorophore, **2TPA-PPDC**, was reported by Zhang *et al.* [23], whose SP-OLEDs emitted at λ_{EL}= 670 nm and showed an $\mathrm{EQE_{max}}$ of 3.2%. A similar red emitter, **DDTPACz-DCPP**, containing carbazole donors that are additionally decorated with two TPA units was reported by Wang *et al.* [24]. The solution-processed devices with **DDTPACz-DCPP** showed $\mathrm{EQE_{max}}$/$\mathrm{EQE_{1000}}$ of 13.6/~4.0% at λ_{EL} of 646 nm. Zeng *et al.* [25] reported an SP-OLED containing the orange-red emitter **NAI_R3** that contains an extended donor moiety and uses *tert*-butylbenzene groups to improve solubility, which emitted at λ_{EL}= 622 nm and showed an $\mathrm{EQE_{max}}$ of 22.5%, but the device also showed a significant efficiency roll-off with an $\mathrm{EQE_{1000}}$ of 3.4%. Liu *et al.* developed a D-A-D type red TADF emitter **TAT-FDBPZ** (Figure 1a) by combining a triazatruxene (TAT) donor and a fluorene-substituted dibenzo[*a*,*c*]phenazine (BP) as the acceptor. The SP-OLED with **TAT-FDBPZ** reached an $\mathrm{EQE_{max}}$ of 9.2% at λ_{EL}= 611 nm and showed a low-efficiency roll-off ($\mathrm{EQE_{1000}}$=7.4%). Using the same BP acceptor, Chen *et al.* [26] developed a D-A type red emitter, **oDBBPZ-DPXZ** (Figure 1a), using two PXZs as donor moieties. SP-OLEDs with **oDBBPZ-DPXZ** emitted at λ_{EL}= 612 nm, and showed an $\mathrm{EQE_{max}}$ of 18.5%; however, efficiency roll-off was severe ($\mathrm{EQE_{1000}}$=~3.0%). This survey of the state-of-the-art in red TADF SP-OLEDs reveals that BP can be used effectively in red emitter design due to its rigid, large π-conjugated system. However, the efficiency of SP-OLEDs using BP-based red emitters still lags behind vacuum-deposited red TADF OLEDs with emitters containing the BP moiety, especially at high luminance (Figure 1a) [27,28].

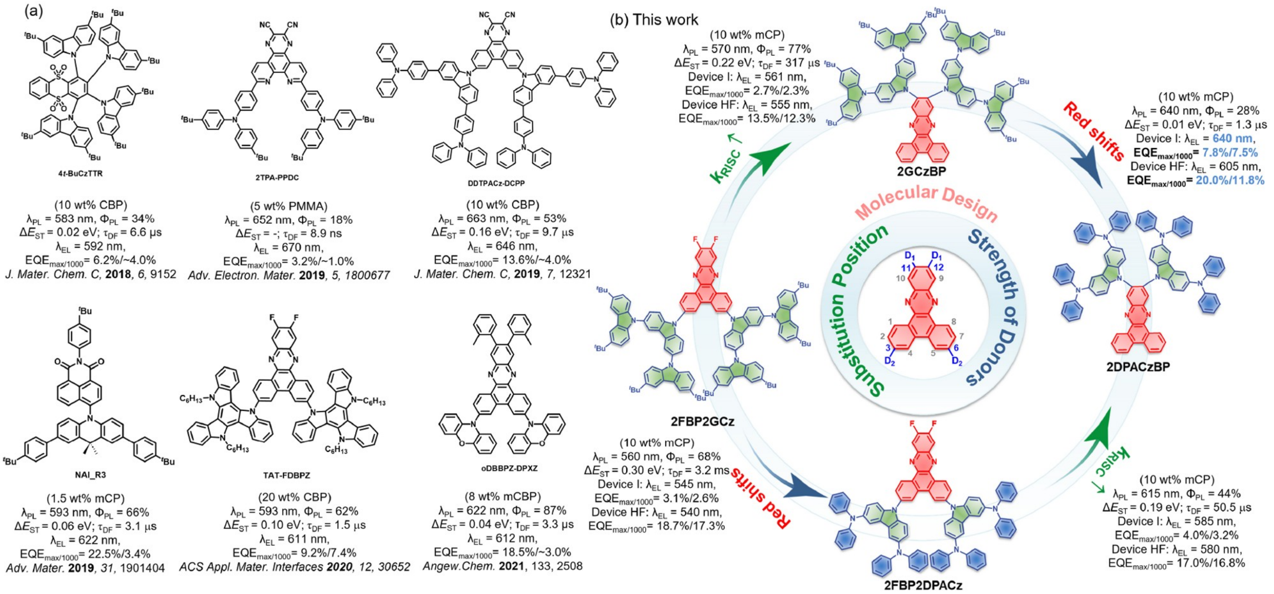

Figure 1 (a) Reported solution-processable red TADF emitter materials. (b) Structures of the dendrimers **2GCzBP**, **2DPACzBP**, **2FBP2GCz** and **2FBP2DPACz** reported in this study based on bespoke second-generation *tert*-butylcarbazole (GCz), N^3,N^3,N^6,N^6-tetraphenyl-9*H*-carbazole-3,6-diamine (DPACz) donor and dibenzo[*a*,*c*]phenazine (BP) acceptor (color online).

Here, we address this issue by employing this rigid BP core as the acceptor and strategically introducing two different donor dendrons, GCz and DPACz, at different positions about the acceptor. We thus report the development of four orange-red TADF dendrimers: 11,12-bis(3,3′′,6,6′′-tetra-*tert*-butyl-9′*H*-[9,3′:6′,9′′-tercarbazol]-9′-yl)dibenzo[*a*,*c*] phenazine (**2GCzBP**), 9,9′-(dibenzo[*a*,*c*]phenazine-11,12-diyl)bis (N^3,N^3,N^6,N^6-tetraphenyl-9*H*-carbazole-3,6-diamine) (**2DPACzBP**), 11,12-difluoro-3,6-bis(3,3′′,6,6′′-tetra-*tert*-butyl-9′H-[9,3′:6′,9′′-tercarbazol]-9′-yl)dibenzo[*a*,*c*]phena-zine (**2FBP2GCz**), and 9,9′-(11,12-difluorodibenzo[*a*,*c*] phenazine-3,6-diyl)bis(N^3,N^3,N^6,N^6-tetraphenyl-9*H*-carbazole-3,6-diamine) (**2FBP2DPACz**) (Figure 1b). We systematically investigated the effect of donor strength and regiochemistry on the optoelectronic properties of the emitters. The reverse intersystem crossing rate constants (k_{RISC}) of **2GCzBP** and **2DPACzBP** are more than 10 times faster than those of **2FBP2GCz** and **2FBP2DPACz**. **2DPACzBP**, containing stronger donors, exhibits a red-shifted emission and smaller singlet-triplet energy splitting, ΔE_{ST}, of 0.01 eV compared with **2GCzBP** which has weaker donors. The SP-OLED with **2DPACzBP** emitted at λ_{EL} = 640 nm, showing an $\mathrm{EQE}_{\max}$ of 7.8% and an EQE_{1000} of 7.5%. The efficiency of the SP-OLEDs could be improved with the introduction of an assistant dopant, **4CzIPN**, in a hyperfluorescence (HF) device configuration. The highest HF device used **2DPACzBP** as the terminal emitter and showed an $\mathrm{EQE}_{\max}$ of 20.0% at λ_{EL} of 605 nm (EQE_{1000} of 11.8%).

2 Experimental

The synthetic routes for **2GCzBP**, **2DPACzBP**, **2FBP2GCz** and **2FBP2DPACz** are shown in Scheme S1 (Supporting Information online). Intermediate **1** was synthesized in 83% yield through the cyclization reaction of 4,5-difluorobenzene-1,2-diamine and phenanthrene-9,10-dione in 1-butanol. **2GCzBP** and **2DPACzBP** were synthesized with good yields (over 80%) through a nucleophilic aromatic substitution reaction between intermediate **1** and dendron GCz, or DPACz, respectively. Intermediates **2** and **3** were obtained by coupling between GCz, DPACz and 3,6-dibromophenanthrene-9,10-dione in yields of 80% and 79%, respectively. The other two final products **2FBP2GCz** and **2FBP2DPACz** were obtained *via* the cyclization reaction of 4,5-difluorobenzene-1,2-diamine and intermediates **2** and **3**, respectively. The identity and purity of the three emitters were verified by proton nuclear magnetic resonance (^{1}H NMR), ^{13}C NMR spectroscopy, melting point determination, high resolution mass spectrometry and elemental analysis and high-performance liquid chromatography (HPLC) (Figures S1–S28, Supporting Information online), with the structure of **2DPACzBP** also being determined by single-crystal X-ray diffraction (XRD).

3 Results and discussion

3.1 X-ray diffraction analysis of 2DPACzBP

Single crystals of **2DPACzBP** were obtained by slow evaporation of a saturated toluene solution at room temperature. **2DPACzBP** adopts a twisted D-A conformation, where the dihedral angles between the BP acceptor and two DPACz donor groups are 62.2° and 65.3° (Figure 2a). Two different C–H···π interactions exist in the compound (Figure 2b), with H···centroid distances of 2.66 and 2.85 Å (corresponding C···centroid separations of 3.429(6) and 3.700(8) Å). Each of these gives rise to a centrosymmetric dimer, which combines to form one-dimensional chains along the [1 −1 0] axis. Neighboring molecules also show weak π···π interactions between the pyrazine and a benzene ring of the BP group (centroid ··· centroid distance of 3.782(3) Å) (Figure 2c), which result in a weakly-interacting chain along the [0 1 0] axis. The two different sets of interactions combine to give a three-dimensional network, which may contribute to the suppression of non-radiative excitonic transitions.

3.2 Theoretical calculations

The ground-state (S_0) geometries of **2GCzBP**, **2DPACzBP**, **2FBP2GCz** and **2FBP2DPACz** were optimized using Density Functional Theory (DFT) at the PBE0 [29]/6-31G(d, p) level [30] in the gas phase starting from a geometry generated in Chem3D [31]. At the optimized S_0 geometries (Figure S29), the dihedral angles between the two donors at the 11 and 12 positions and the acceptor moiety in **2GCzBP**

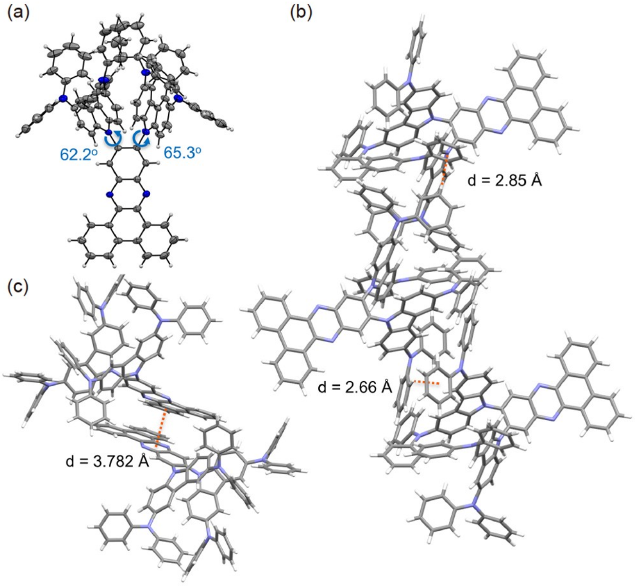

Figure 2 (a) Thermal ellipsoid plot of one independent molecule in the single crystal structure of **2DPACzBP**. Ellipsoids are drawn at the 50% probability level and solvent molecules have been omitted for clarity; (b) view of C–H···π interactions in the compound and (c) view showing π···π interactions between adjacent molecules (color online).

(~67°) and **2DPACzBP** (~58°) are much larger than those with the alternative donors at the 3 and 6 positions in **2FBP2GCz** (~43°) and **2FBP2DPACz** (~44°); calculations reproduce the degree of twisting observed in the crystal structure of **2DPACzBP**. This divergence in behavior results from larger steric hindrance between the donors in **2GCzBP** and **2DPACzBP**. The calculated energy levels of the highest occupied molecular orbitals (HOMOs) and lowest unoccupied molecular orbitals (LUMOs) are shown in Figure 3a and Figure S30. The HOMOs are localized on the donors, while the LUMOs are localized on the BP acceptor group. As the donor strength increases from **2GCzBP** to **2DPACzBP** and from **2FBP2GCz** to **2FBP2DPACz**, the HOMOs are destabilized. As expected, the LUMOs are also destabilized with increasing donor strength from **2GCzBP** to **2DPACzBP**, given the electronic coupling between the donor and acceptor groups. When using the same donor, the LUMO of **2GCzBP** is slightly deeper than that of **2FBP2GCz**. This due in part to the two inductively electron-withdrawing fluorine atoms in the acceptor of **2FBP2GCz**. The HOMO of **2GCzBP** (−5.19 eV) is more destabilized compared with that of **2FBP2GCz** (−5.40 eV). This destabilization is attributed to the presence of two donors at adjacent positions exhibiting a cooperative effect, where their combined electronic influence is greater than the sum of their individual effects in **2FBP2GCz**. So, the overall electron-donating ability of **2DPACzBP** is amplified, leading to a more destabilized HOMO. The HOMO-LUMO gap, $\Delta E_{\text{HOMO-LUMO}}$, thus decreases from 2.50 eV for **2GCzBP** to 2.38 eV for **2DPACzBP**, while the $\Delta E_{\text{HOMO-LUMO}}$ decreases from 2.72 eV in **2FBP2GCz** to 2.50 eV in **2GCzBP**.

The excited-state properties were calculated using time-dependent DFT (TD-DFT) within the Tamm-Dancoff approximation (TDA-DFT) [32] based on the optimized ground-state geometries (Figure 3a). The oscillator strength, *f*, for the $S_0 \rightarrow S_1$ transition of **2GCzBP**, **2DPACzBP**, **2FBP2GCz** and **2FBP2DPACz** is 0.06, 0.01, 0.10 and 0.08, respectively, reflecting the relatively smaller torsions and thus greater conjugation that exist between the position 3, 6 donors and the acceptor moieties in **2FBP2GCz** and **2FBP2DPACz**. The S_1 energies are 2.09 eV for **2GCzBP**, 1.95 eV for **2DPACzBP**, 2.42 eV for **2FBP2GCz** and 2.10 eV for **2FBP2DPACz**, while the corresponding T_1 energies are 2.04,1.87,2.32 and 2.02 eV, respectively, both following a similar trend to that observed for $\Delta E_{\text{HOMO-LUMO}}$ values (Figure 3a). All four compounds have small predicted ΔE_{ST} of less than 0.10 eV, suggesting that these compounds should emit *via* TADF. There is a larger S_1-T_1 spin-orbital coupling matrix element, SOCME, in **2FBP2GCz** (0.19 cm^{-1}) and in **2GCzBP** (0.10 cm^{-1}) than that in **2FBP2DPACz** (0.09 cm^{-1}) and **2DPACzBP** (0.06 cm^{-1}) (Figure 3a), indicating that the ISC will likely be faster in **2FBP2GCz** and **2GCzBP** than that in the other two compounds. Natural transition orbital (NTO) analyses at the S_0-optimized geometry (Figure 3b) demonstrated that the low-lying excited states in all four compounds possess charge transfer (CT) characteristics. Holes and electrons are well separated on the donor and acceptor moieties, respectively. There is a somewhat smaller separation in the T_1 state of **2FBP2GCz** and **2FBP2DPACz**, so this state in these two

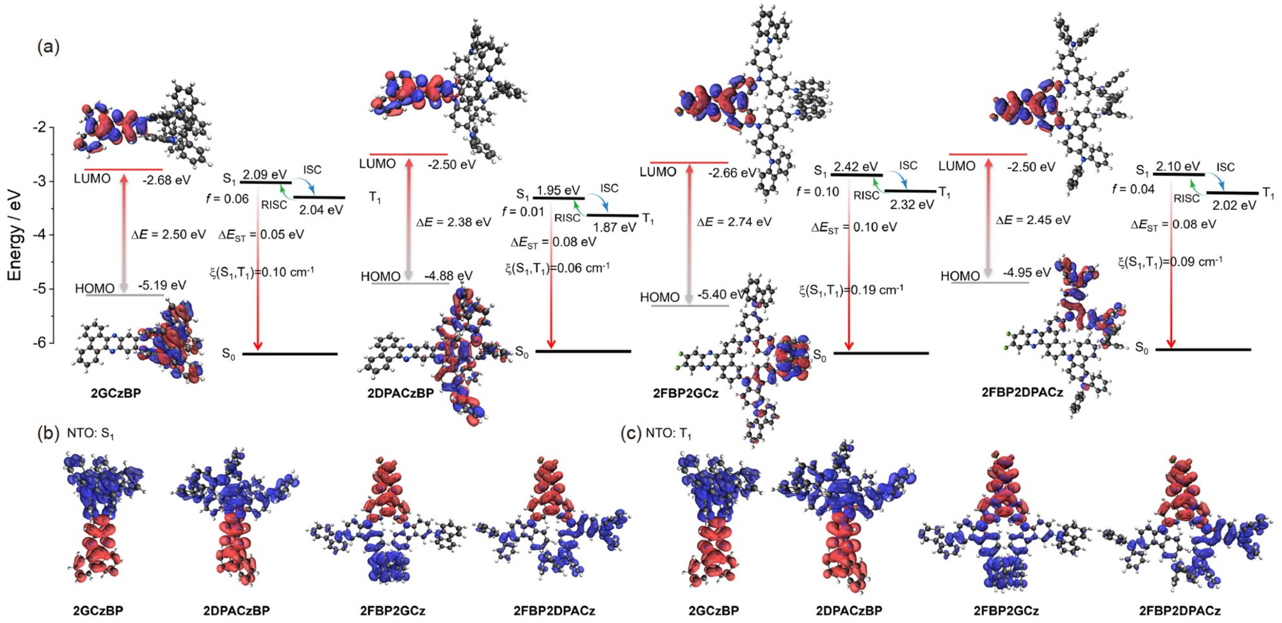

Figure 3 (a) Frontier molecular orbitals (isovalue: 0.02) and vertical excitation energy levels calculated at the optimized S_0 geometry in the gas phase at the PBE0/6-31G(d,p) level. Natural transition orbitals (unoccupied (hole, blue) & occupied (electron, red), (isovalue: 0.02)) of (b) S_1 and (c) T_1 for **2GCzBP**, **2DPACzBP**, **2FBP2GCz** and **2FBP2DPACz** calculated at the optimized S_0 geometry in the gas phase at the PBE0/6-31G(d,p) level (color online).

compounds is better described as a mixture of locally excited (LE) and CT character (Figure 3c).

3.3 Electrochemistry

The energies of the frontier molecular orbitals (FMOs) were inferred from the electrochemical behavior of **2GCzBP**, **2DPACzBP**, **2FBP2GCz,** and **2FBP2DPACz** by cyclic voltammetry (CV) and differential pulse voltammetry (DPV) in degassed dichloromethane (DCM) with tetra-*n*-butylammonium hexafluorophosphate, $[^n\mathrm{Bu_4N}]\mathrm{PF_6}$, as the supporting electrolyte (Figure 4a) [33]. The reduction potentials (E_red), determined from the DPV peak values, are −1.24 V (**2GCzBP**), −1.38 V (**2DPACzBP**), −1.28 V (**2FBP2GCz**) and −1.35 V (**2FBP2DPACz**) reflecting the expected cathodic shift with the increase in donor strength. The LUMO energies are –3.11,−3.07,−3.08, and −3.02 eV for **2GCzBP**, **2DPACzBP**, **2FBP2GCz** and **2FBP2DPACz**, respectively, and align with the trend found for the DFT calculations (Figure 3a). **2GCzBP** and **2FBP2GCz** both have two resolvable quasi-reversible oxidation waves, with similar first oxidation potentials at E_ox of 1.03 V, and second oxidation potentials at 1.13 V, which correspond to the oxidation of the inner carbazole and the peripheral *tert*-butylcarbazole, respectively [9,34]. A similar trend is observed for **2DPACzBP** (E_ox = 0.66 V) and **2FBP2DPACz** (E_ox = 0.65 V). The HOMO levels of **2GCzBP**, **2DPACzBP**, **2FBP2GCz** and **2FBP2DPACz** are −5.38, −5.01, −5.37 and −5.02 eV, respectively. The electrochemical data indicate that compounds with the same donors have effectively the same E_ox. However, this behavior is not reproduced in the DFT calculations where the calculated HOMO of **2FBP2GCz** (–5.40 eV) is more stabilized than that of **2GCzBP** (–5.19 eV). The corresponding HOMO-LUMO gaps are 2.27, 2.04, 2.30 and 2.00 eV, for **2GCzBP**, **2DPACzBP**, **2FBP2GCz** and **2FBP2DPACz**, respectively, which mirror the trend in the DFT calculated values of 2.50, 2.38, 2.74, 2.45 eV.

3.4 Photophysical properties

The ultraviolet-visible spectroscopy (UV-Vis) absorption spectra of the four emitters in dilute toluene are shown in Figure 4b, and the photophysical properties are summarized in Table 1. All four compounds exhibit strong absorption bands below 400 nm (**2GCzBP** (346 nm, ε=5.7×10^4 M^{-1} cm^{-1}), **2DPACzBP** (353 nm, ε=3.3×10^4 M^{-1} cm^{-1}), **2FBP2GCz** (348 nm, ε=4.7×10^4 M^{-1} cm^{-1}) and **2FBP2DPACz** (354 nm, ε=4.1×10^4 M^{-1} cm^{-1})), which are attributed to LE π-π* transitions of both the donors and acceptor moieties based on a comparison with literature data of BP and GCz [9,10,26]. Weaker and broader absorption bands are observed at 460 nm (ε=1.6×10^4 M^{-1} cm^{-1}) for **2GCzBP**, 506 nm (ε=0.7×10^4 M^{-1} cm^{-1}) for **2DPACzBP**, 436 nm (ε=1.4×10^4 M^{-1} cm^{-1}) for **2FBP2GCz** and 464 nm (ε=1.1×10^4 M^{-1} cm^{-1}) for **2FBP2DPACz**, which are assigned to ICT transitions from the donor units to the acceptor core, assignments that are corroborated by the relative oscillator strengths (*f* = 0.04, 0.01, 0.10 and 0.04 for **2GCzBP**, **2DPACzBP**, **2FBP2GCz** and **2FBP2DPACz**, respectively) calculated by TDA-DFT (Figure 3 and Figure S31). There is an expected shift to lower energies of the ICT band aligned with increasing donor strength (from **2GCzBP** to **2DPACzBP**) and donor substitution position from positions 3 and 6 to positions 11 and 12 (**2FBP2GCz** to **2GCzBP**). All compounds exhibit unstructured and broad photoluminescence (PL) spectra in toluene (Figure 4b), indicative of an excited state with strong ICT character, with peak maxima τ_PL, at 585, 690, 565, and 675 nm for **2GCzBP**, **2DPACzBP**, **2FBP2GCz** and **2FBP2DPACz**, respectively. Positive solvatochromism is observed for all compounds (Figure 4c), which is consistent with the ICT nature of the emissive excited state. The structured higher energy emission band for **2FBP2DPACz** in

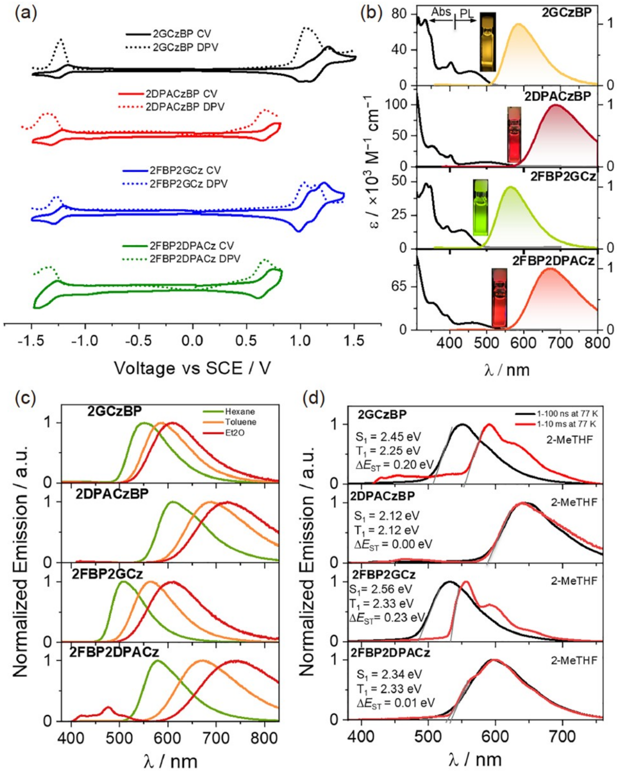

Figure 4 (a) Cyclic and differential pulse voltammograms measured in degassed DCM with 0.1 M $[^n\mathrm{Bu_4N}]\mathrm{PF_6}$ as the supporting electrolyte and Fc/Fc$^+$ as the internal reference (0.46 V *vs*. SCE) [33]. Scan rate: 100 mV s^{-1}. (b) UV-Vis absorption (in toluene) and steady-state photoluminescence (PL) spectra of **2GCzBP**, **2DPACzBP**, **2FBP2GCz** and **2FBP2DPACz** recorded in toluene at room temperature (λ_exc=340 nm). (c) PL solvatochromism study of **2GCzBP**, **2DPACzBP**, **2FBP2GCz** and **2FBP2DPACz** recorded at room temperature (λ_exc=340 nm). (d) Prompt fluorescence (1–100 ns) and phosphorescence spectra (1–10 ms) in 2-MeTHF at 77 K of **2GCzBP**, **2DPACzBP**, **2FBP2GCz** and **2FBP2DPACz** (λ_exc = 343 nm) (color online).

Et_2O is attributed to originating from an LE state of the donor, as it closely matches the DPACz emission in spectral shape and energy (Figure S32).

The optical bandgaps, E_g, calculated from the normalized absorption and emission spectra intersection point, are 2.38, 2.09, 2.54, and 2.21 eV for **2GCzBP**, **2DPACzBP**, **2FBP2GCz** and **2FBP2DPACz**, respectively (Figure S33), roughly consistent with the trend in electrochemical redox gaps (Table 1). The Φ_{PL} values in degassed toluene solution are 59%, 6%, 47% and 9%, respectively, for **2GCzBP**, **2DPACzBP**, **2FBP2GCz** and **2FBP2DPACz**. When exposed to oxygen, these values significantly decrease to 38% and 27% for **2GCzBP** and **2FBP2GCz**, respectively, and slightly decrease to 5%, and 5% for **2DPACzBP** and **2FBP2DPACz**. The lower Φ_{PL} of **2DPACzBP** and **2FBP2DPACz** may be due in part to the non-radiative decay channels emanating from the more flexible DPACz donor as well as the energy-gap law [35], which states that the non-radiative decay rate increases exponentially as the energy gap decreases. The prompt fluorescence and phosphorescence spectra in 2-MeTHF glass at 77 K were measured to determine the S_1 and T_1 energies from their respective onsets (Figure 4d). The S_1 energies of **2GCzBP**, **2DPACzBP**, **2FBP2GCz** and **2FBP2DPACz** are 2.45, 2.12, 2.56, and 2.34 eV, and the T_1 energies are 2.25, 2.12, 2.33, and 2.33 eV, respectively. The observed trends for both S_1 and T_1 energy levels align with the computational data presented in Figure 3b. The phosphorescence spectra of **2GCzBP** and **2FBP2GCz** are structured, and each is assigned from TDA-DFT calculations as a mixed locally excited triplet (^{3}LE) state of the acceptor (BP-F) and charge-transfer (^{3}CT) state (Figure 3d). The ΔE_{ST} of **2GCzBP**, **2DPACzBP**, **2FBP2GCz** and **2FBP2DPACz** are 0.20, 0.00, 0.23, and 0.01 eV, respectively, which are similar to the trend in the calculated values, where **2FBP2GCz** has the largest calculated ΔE_{ST} of 0.10 eV compared with **2GCzBP** (0.04 eV), **2DPACzBP** (0.08 eV) and **2FBP2DPACz** (0.08 eV), as shown in Figure 3b.

The PL decays of the four compounds in toluene under degassed conditions were measured using a combination of time-correlated single-photon counting/multi-channel scanner (TCSPC/MCS) techniques (Figure S34). The ICT bands of **2GCzBP**, **2DPACzBP**, **2FBP2GCz** and **2FBP2DPACz** all decay with biexponential kinetics, with prompt fluores-

Table 1 Photophysical properties of 2GCzBP, 2DPACzBP, 2FBP2GCz and 2FBP2DPACz

Properties	2GCzBP	2DPACzBP	2FBP2GCz	2FBP2DPACz
λ_{abs} (ε ×10^3 M^{-1} cm^{-1})$^{a)}$ (nm)	346 (57), 460(16)	353 (33), 403(18), 506(7)	348 (47), 394(17), 436(14)	354(41), 394(22), 464(11)
$\lambda_{PL}$$^{a)}$ (nm)	585	690	565	675
$S_1/T_1$$^{b)}$ (eV)	2.45/2.25	2.12/2.12	2.56/2.33	2.34/2.33
$\Delta E_{ST}$$^{b)}$ (eV)	0.2	0	0.23	0.01
$\lambda_{PL}$$^{c)}$ (nm)	570	640	560	615
$\Phi_{PL}$$^{c)}$ (%)	77 (68)	28 (27)	68 (53)	44 (41)
$\tau_p$$^{d)}$ (ns)	22.9	15.6	21.1	23
$\tau_d$$^{d)}$ (μs)	317	1.3	3200	50.5
$S_1/T_1$$^{e)}$ (eV)	2.49/2.27	2.17/2.16	2.65/2.35	2.42/2.23
ΔE_{ST} (eV)	0.22	0.01	0.3	0.19
$k_{ISC}$$^{f)}$ (×10^7 s^{-1})	0.52	0.23	1.12	0.29
$k_{RISC}$$^{f)}$ (×10^4 s^{-1})	0.36	79.8	0.04	2.13
$k_{sr}$$^{f)}$ (×10^7 s^{-1})	2.96	1.73	2.51	1.78
$k_{snr}$$^{f)}$ (×10^7 s^{-1})	0.88	4.45	1.18	2.27
HOMO$^{g)}$ (eV)	–5.38	–5.01	–5.37	–5.02
LUMO$^{g)}$ (eV)	–3.11	–2.97	–3.07	–3.02
$E_g$$^{h)}$ (eV)	2.27	2.04	2.3	2

a) In PhMe at 298 K (λ_{exc}=340 nm). b) Obtained from the onset of the prompt fluorescence (time window: 1–100 ns) and phosphorescence spectra (time window: 1–10 ms) measured in 2-MeTHF glass at 77 K, λ_{exc} = 343 nm. c) Thin films of 10 wt% emitters doped in mCP were prepared by spin-coating, and Φ_{PL} values were determined using an integrating sphere (λ_{exc} = 340 nm). Values quoted are under N_2. Values in parentheses are in the air. d) PL lifetimes were measured by TCSPC and MCS, respectively (λ_{exc} = 379 nm). e) S_1 was obtained from the onset of the prompt emission (time-gated window: 1–100 ns) measured in doped film at 77 K and T_1 was obtained from the onset of the phosphorescence spectrum (time-gated window: 1–10 ms) measured in doped film at 77 K. f) k_{ISC} = intersystem crossing rate from S_1 to T_1 states; k_{RISC} = reverse intersystem crossing rate. g) In DCM with 0.1 M [^{n}Bu$_4$N]PF$_6$ as supporting electrolyte and Fc/Fc$^+$ as the internal reference (0.46 V *vs*. SCE) [33]. The HOMO and LUMO energies were determined using $E_{HOMO/LUMO=} - (E_{ox}/\ E_{red} + 4.8)$ eV where E_{ox} and E_{red} are anodic and cathodic peak potentials, respectively, obtained from the DPV [33]. h) $E_g = |E_{HOMO} - E_{LUMO}|$.

cence lifetimes, τ_p, of 22.2, 4.2, 14.2, and 3.2 ns, and delayed fluorescence lifetimes, τ_d, of 79.1, 0.24, 102.6, and 0.25 μs, respectively. The corresponding rate constants for intersystem crossing (k_{ISC}) for **2GCzBP**, **2DPACzBP**, **2FBP2GCz** and **2FBP2DPACz** are 1.0×10^7, 3.9×10^7, 3.0×10^7, and 1.4×10^8 s^{-1}, respectively, while the rate constants for reverse intersystem crossing (k_{RISC}) for **2DPACzBP** (5.0×10^6 s^{-1}) and **2FBP2DPACz** (7.3×10^6 s^{-1}) are much faster than those of **2GCzBP** (1.6×10^4 s^{-1}) and **2FBP2DPACz** (1.4×10^4 s^{-1}), due in part to the smaller ΔE_{ST} in the former two. However, **2DPACzBP** and **2FBP2DPACz** also possess much faster non-radiative decay rate constants (k_{nr}) at 1.9×10^8 and 1.6×10^8 s^{-1}, respectively, than those of **2GCzBP** ($k_{nr} = 1.4 \times 10^7$ s^{-1}) and **2FBP2DPACz** ($k_{nr} = 2.1 \times 10^7$ s^{-1}), which we attribute to a direct consequence of the energy gap law [35]. The delayed components of **2GCzBP** and **2FBP2GCz** are much longer-lived and were totally quenched by oxygen, reflective of the larger ΔE_{ST} in these two compounds. The corresponding PL intensity of toluene solutions was enhanced upon the oxygen removal for all four compounds (Figure S34e, f), demonstrating that oxygen could quench triplet states.

We next assessed the photophysical properties of these emitters in an OLED-relevant host 1,3-bis(*N*-carbazolyl) benzene (mCP), as this host matrix has sufficiently high triplet energy ($T_1 = 2.91$ eV) to confine the excitons onto the emitter [25]. Figure 5a shows the PL spectra of the 1 wt% and 10 wt% doped films in mCP and the neat film. The emission spectra gradually red-shifted by up to 10 nm as the doping concertation increased from 1 wt% to 10 wt%, while the red-shift was more pronounced at over 50 nm in neat films due to strong intermolecular interactions [36]. The optimized doping concentration for **2GCzBP**, **2DPACzBP**, **2FBP2GCz** and **2FBP2DPACz** was determined to be 10 wt% as a function of Φ_{PL} (Figure S35 and Table S1, Supporting Information online), and the corresponding Φ_{PL} values under an N_2 atmosphere are 77%, 28%, 68%, and 44%, respectively, which decrease to 68%, 27%, 53%, and 41%, respectively, under air. The Φ_{PL} values of all four compounds increased compared with those in toluene due to a combination of suppressed non-radiative decay in the solid host and efficient Förster resonance energy transfer (FRET) from host to dopant emitters [37]. The PL spectra of the 10 wt% doped films in mCP, are all unstructured, with λ_{PL} at 570, 640, 560, and 615 nm for **2GCzBP**, **2DPACzBP**, **2FBP2GCz** and **2FBP2DPACz**, respectively (Figure 5a, Table 1), values that are slightly blue-shifted compared with those in toluene (**2GCzBP** (585 nm), **2DPACzBP** (690 nm), **2FBP2GCz** (565 nm) and **2FBP2DPACz** (675 nm), Figure 4b). It has been demonstrated that the emission color of the compounds is influenced not only by the strength of the donor but also their regiochemistry, undergoing a significant red-shift when the same donors are substituted at positions 11/12 instead of positions 3/6 on the BP acceptor.

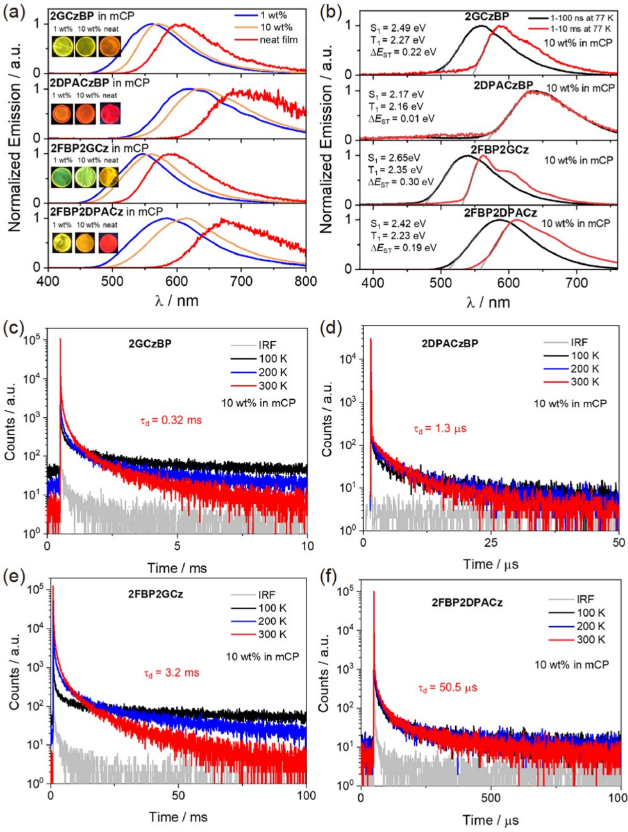

Figure 5 (a) Steady-state PL spectra of **2GCzBP**, **2DPACzBP**, **2FBP2GCz** and **2FBP2DPACz** recorded in doped mCP film at room temperature (λ_{exc} = 340 nm). (b) Prompt fluorescence (1–100 ns) and phosphorescence spectra (1–10 ms) in 10 wt% doped films in mCP at 77 K of **2GCzBP**, **2DPACzBP**, **2FBP2GCz** and **2FBP2DPACz** (λ_{exc} = 343 nm). Temperature-dependent time-resolved PL decay of 10 wt% (c) **2GCzBP**, (d) **2DPACzBP**, (e) **2FBP2GCz** and (f) **2FBP2DPACz** doped films in mCP (λ_{exc}= 379 nm) (color online).

The S_1/T_1 energy levels of **2GCzBP** (2.45/2.25 eV), **2DPACzBP** (2.12/2.12 eV), **2FBP2GCz** (2.56/2.33 eV) and **2FBP2DPACz** (2.34/2.33 eV) of the 10 wt% doped films in mCP were estimated from the onsets of the fluorescence and phosphorescence spectra at 77 K (Figure 5b). The corresponding ΔE_{ST} values of **2GCzBP**, **2DPACzBP**, **2FBP2GCz** and **2FBP2DPACz** are 0.22, 0.01, 0.30, and 0.19 eV, respectively, align with similar results acquired in 2-MeTHF at 77 K. Similar to those in toluene, the fluorescence spectra are all unstructured, indicating emission from ^{1}CT, while the phosphorescence spectra of **2GCzBP** and **2FBP2GCz** are structured, assigned to emission from the ^{3}LE state of the acceptor. As shown in Figure 5c, d, all four compounds showed multiexponential decay kinetics with average prompt fluorescence lifetimes, average τ_p, of 22.9, 15.6, 21.1, and 23.0 ns, and average delayed emission lifetimes, average τ_d, of 0.3 ms,1.3 μs,3.2 ms and 50.5 μs at room temperature for **2GCzBP**, **2DPACzBP**, **2FBP2GCz** and **2FBP2DPACz**, respectively. From these average values, the estimated k_{ISC} for the four compounds are 0.52 × 10^7, 0.23 × 10^7, 1.12 × 10^7, and 0.29 × 10^7 s^{-1} for **2GCzBP**, **2DPACzBP**, **2FBP2GCz** and **2FBP2DPACz**, respectively, while the estimated k_{RISC} for **2DPACzBP** reached 7.98 × 10^5 s^{-1}, a value much faster than for **2GCzBP** of 0.36 × 10^4 s^{-1},**2FBP2GCz** of 0.04 × 10^4 s^{-1} and **2FBP2DPACz** of 2.13 × 10^4 s^{-1}, respectively. Liu *et al*. [38] reported a similar TADF emitter, **TAT-FDBPZ** (Figure 1), that contains two triazatruxene donors and the same acceptor as **2FBP2GCz/2FBP2DPACz**. **TAT-FDBPZ** emits at λ_{PL} of 593 nm, has a much shorter τ_{d} of 1.51 μs and faster k_{RISC} of 1.71 × 10^6 s^{-1} than those of **2FBP2GCz/2FBP2DPACz**, which could result from the more rigid and conjugated structure of TAT than those of GCz and DPACz used in our work. For the same donor, the k_{RISC} for the compounds substituted in 11/12 positions is more than 10 times faster than that of the compounds substituted in 3/6 positions due to the smaller ΔE_{ST}. For compounds with the same substitution pattern, the k_{RISC} for the compounds substituted by the stronger DPACz donors is more than 50 times faster than that of compounds with weaker GCz donors due to its smaller ΔE_{ST}. Xie *et al*. [39] reported a TADF molecule, **2DMAC-BP**, containing two DMAC donors attached to the BP acceptor, which emits at λ_{PL} of 553 nm, has a τ_{d} of 7.5 μs and k_{RISC} of 4.74 × 10^5 s^{-1} in 20 wt% doped films in mCBP, thereby having a k_{RISC} that is around half that of **2DPACzBP** (k_{RISC} = 7.98 × 10^5 s^{-1}). Zeng *et al*. [40] developed another TADF emitter **DPPZ-2DMAC**, which consists of a similar acceptor to BP and two DMAC donors substituted at the 10 and 11 positions. Similar to what was observed in **2DMAC-BP**, **DPPZ-2DMAC** exhibits a red-shifted emission of λ_{PL}= 620 nm and has shorter τ_{d} of 4.5 μs and fast k_{RISC} of 5.52 × 10^5 s^{-1} that is nonetheless slower than that of **2DPACzBP**. Finally, as shown in Figure 5c, d, the relative intensities of the delayed PL increase with increasing temperature from 100 to 300 K, thereby corroborating the TADF nature of the emission of these four compounds in the 10 wt% films in mCP.

3.5 Device characterization

To evaluate the electroluminescent (EL) performance of these emitters, solution-processed OLEDs employing 10 wt % emitters doped in mCP films as the emissive layer (EML) were fabricated with a typical configuration of indium ITO (indium tin oxide)/poly(3,4-ethylenediox ythiophene):poly (styrenesulfonate) (PEDOT:PSS) (40 nm)/ mCP:10 wt% dopant (20 nm)/TmPyPB (3,3′-(5′-(3-(pyridin-3-yl)phenyl)-[1,1′:3′,1″-terphenyl]-3,3″-diyl)dipyridine) (45 nm)/LiF (1 nm)/Al (Figure 6 and Figure S36), where ITO and Al serve as the anode and cathode, respectively. PEDOT:PSS and TmPyPB are sequentially used as the hole-transporting layer and electron-transporting layer, respectively. As shown in Figure S36, the OLEDs with **2FBP2GCz**, **2GCzBP**, **2FBP2DPACz** and **2DPACzBP** at doping concertation of 10 wt% in mCP host exhibit green, yellow to pure red emission with the electroluminescence peaks, λ_{EL}, at 545, 561, 585 and 640 nm, and corresponding Commission Internationale de L'Éclairage (CIE) coordinates of (0.37, 0.57), (0.46, 0.53), (0.51, 0.48) and (0.61, 0.36) in the device, which match the PL emission very well (Figures 5a). As

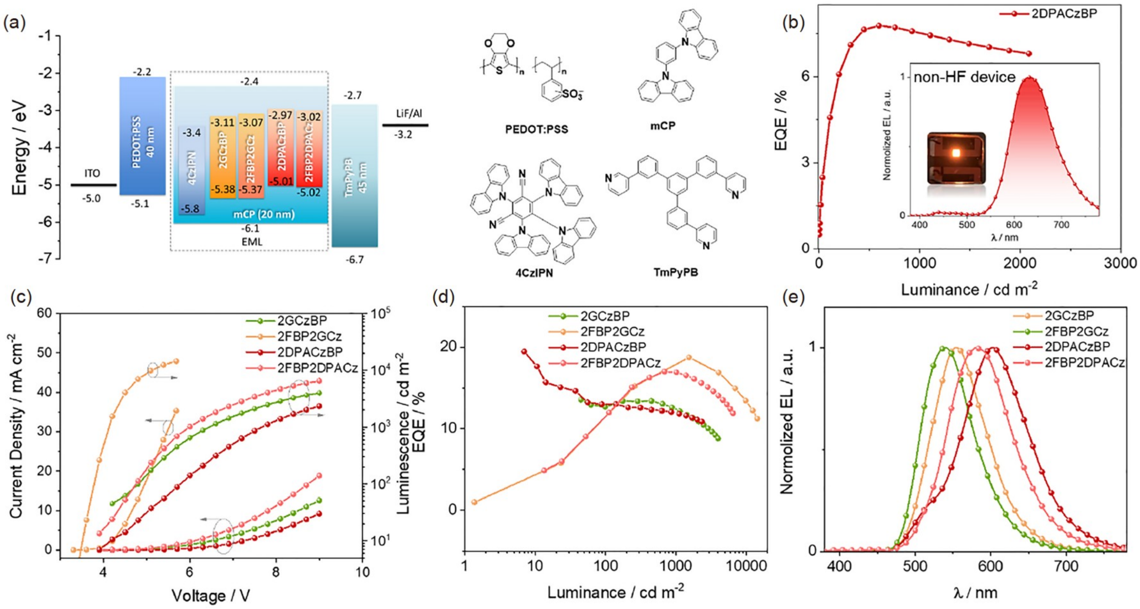

Figure 6 (a) Energy level diagram and molecular structure of materials employed in the HF devices. (b) External quantum efficiency *versus* luminance curves and EL spectra of for **2DPACzBP**-based device with the structure of ITO/PEDOT:PSS (40 nm)/mCP:10 wt% dopants (20 nm)/TmPyPB (45 nm)/LiF (1 nm)/Al. (c) Current density and luminance versus voltage characteristics for the HF devices. (d) External quantum efficiency *versus* luminance curves for the HF devices. (e) Electroluminescence spectra of the HF devices (color online).

depicted in Figure 6b, the devices with **2DPACzBP** showed the highest EQE_{max} of 7.8% at 600 cd m^{-2} (Figure 7a) and negligible efficiency roll-off at 1,000 cd m^{-2} (EQE_{1000}= 7.6%), which is the highest EQE_{1000} in reported red solution-processed OLEDs to date (Figure 7b and Table 2 and Table S2), and maintains 87% of its EQE_{max} at 2,000 cd m^{-2} (EQE_{2000}= 6.8%).

To improve the efficiency of the devices, we next explored the fabrication of TADF-sensitized-fluorescence, or hyperfluorescence (HF), devices (Figure 6a) [41]. Here, **4CzIPN** was selected as the TADF assistant dopant because of its high Φ_{PL}, short τ_d in mCP [42–44], and a strong spectral overlap between the absorption spectra of these four emitters and the PL spectrum of **4CzIPN** in toluene (Figure S37). The optimized ratio of emitters/4CzIPN/mCP was established in the literature to be 3:32:65 [41,45,46]. The device performance is shown in Figure 6c–e, and the data are summarized in Table 2. As shown in Figure 6e, the EQEs of the HF devices with all four compounds have been greatly improved compared with the previous set of devices. The HF devices with **2DPACzBP** showed an enhanced EQE_{max} of 20.0% at λ_{EL}= 605 nm (Figure 7a), much higher than 7.8% in the non-HF devices. However, a noticeable blue shift in the EL spectra was observed, moving from λ_{EL} = 640 nm (no-HF devices) to λ_{EL}= 605 nm in HF devices, which we attributed to the lower doping concertation of the emitter in the EML. The HF devices with **2FBP2GCz**, **2GCzBP** and **2FBP2DPACz** showed higher EQE_{max} of 18.7%, 13.5% and 17.0% with blue-shifted EL spectra λ_{EL} at 540, 555 and 580 nm, respectively, than their respective non-HF devices. The EQE_{1000} in the HF devices with **2FBP2GCz**, **2GCzBP**, **2FBP2DPACz** and **2DPACzBP** still remained reasonably high at 17.3%, 12.3%, 16.8% and 11.8%, respectively (Table 2), which, to the best of our knowledge, is amongst the best performance for orange to red HF SP-OLED to date (Figure 7, Table S2). Although **2DPACzBP** possesses the fastest k_{RISC} among these four compounds, the OLED with **2DPACzBP** showed a serious efficiency roll-off at high luminance, which may nonetheless be linked to bimolecular quenching processes [47–49], such as triplet-triplet and tri-

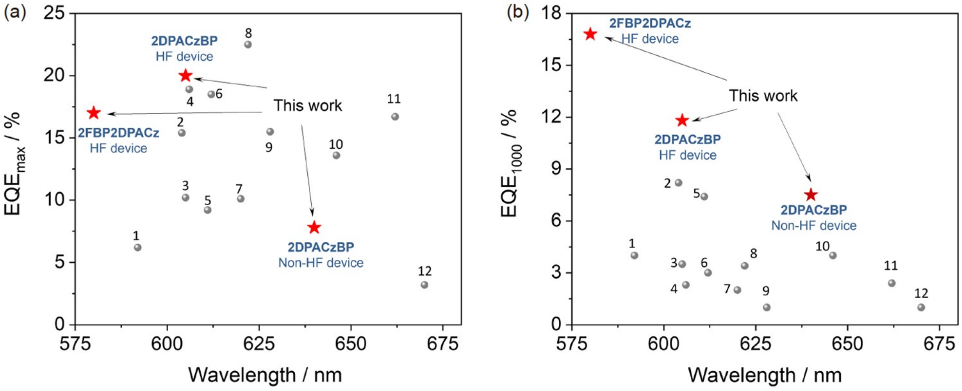

Figure 7 (a) The EQE_{max} values and (b) EQE values at 1,000 cd m^{-2} of all reported orange-to-red solution-processed (λ_{EL} > 575 nm) TADF OLEDs as a function of wavelength (Table S2) (color online).

Table 2 Device electroluminescence data

Emitter	Host	V_{on} $^{a)}$ (V)	λ_{EL} $^{b)}$ (nm)	CE (cd A^{-1})	PE_{max} (lm W^{-1})	EQE$^{c)}$ (%)	CIE$^{d)}$ (*x*, *y*)
2GCzBP	mCP (10%)	3.9	561	8.8	3.1	2.7/1.1/2.3	0.46, 0.53
2FBP2GCz	mCP (10%)	3.0	545	10.3	3.8	3.1/1.0/2.6	0.37, 0.57
2DPACzBP	mCP (10%)	3.4	640	9.6	4.9	7.8/4.6/7.5	0.61, 0.36
2FBP2DPACz	mCP (10%)	3.2	585	10.8	3.8	4.0/1.4/3.2	0.51, 0.48
2GCzBP	mCP:4CzIPN (65%:32%) (3%)	3.9	555	49.0	36.6	13.5/13.1/12.3	0.41, 0.57
2FBP2GCz	mCP:4CzIPN (65%:32%) (3%)	3.0	540	68.2	51.0	18.7/11.2/17.3	0.34, 0.60
2DPACzBP	mCP:4CzIPN (65%:32%) (3%)	3.4	605	46.1	36.7	20.0/13.1/11.8	0.53, 0.45
2FBP2DPACz	mCP:4CzIPN (65%:32%) (3%)	3.2	580	49.5	27.3	17.0/11.3/16.8	0.49, 0.49

a) The turn-on voltage at a brightness ≈ 1 cd m^{-2}. b) The electroluminescence maximum recorded at 6 V. c) EQE_{max}/EQE_{100}/ EQE_{1000}. d) The CIE coordinates recorded at 6 V.

plet-polaron annihilation induced by charge carrier imbalance in the emissive layer.

4 Conclusions

Here, we designed and synthesized four novel orange-red solution-processable TADF dendrimers, **2GCzBP**, **2DPACzBP**, **2FBP2GCz** and **2FBP2DPACz**. We systematically investigated the effect of substitution position and strength of the donors on their optoelectronic properties. From this study, we can draw the following conclusions. (1) The emission color of the compounds not only depends on the donor strength but also shows a large red shift when the same donors are substituted from position 3/6 to position 11/12 of the BP acceptor. (2) The k_{RISC} for the compounds substituted in positions 11 and 12 of BP is more than ten times faster than that of compounds substituted in positions 3 and 6. (3) **2GCzBP** exhibits the highest Φ_{PL} of 77%, and the Φ_{PL} slightly decreases to 68% for **2FBP2GCz**, wherein both compounds have donors at the 3 and 6 positions. However, both **2DPACzBP** and **2FBP2DPACz** have much lower Φ_{PL}, which we attribute to a consequence of the energy gap law, especially for **2DPACzBP** (the smallest S_1 and lowest Φ_{PL}). (4) Due to the larger dihedral angles between the donors at the 11/12 positions and the acceptor, **2GCzBP** and **2DPACzBP** possess much smaller ΔE_{ST} compared with their respective analogs, **2FBP2GCz** and **2FBP2DPACz**. Furthermore, the stronger donor contributes to the smaller ΔE_{ST} in these compounds with the same substitution position. The SP-OLED with **2DPACzBP** emitted at λ_{EL}= 640 nm and showed an $\mathrm{EQE}_{\max}$ of 7.8% and a low-efficiency roll-off where the EQE remains high at 7.5% at a luminance of 1,000 cd m^{-2}, which is among the best results for red solution-processed TADF OLEDs at this luminance. The much worse performance for the devices with **2GCzBP**, **2FBP2GCz** and **2FBP2DPACz** may be linked to a combination of their slower k_{RISC} and their having an unoptimized device structure. The efficiency of the HF devices using **4CzIPN** as the assistant dopant improved significantly, where the **2DPACzBP** HF device showed a particularly attractive performance with an $\mathrm{EQE}_{\max}$ of 20.0% at λ_{EL} = 605 nm, which is the best performance for the orange-to-red HF SP-OLED.

Acknowledgements Changfeng Si thanks the China Scholarship Council (201806890001). Dianming Sun acknowledges support from the Royal Academy of Engineering Enterprise Fellowship (EF2122-13106). We thank EPSRC (EP/W015137/1, EP/W524505/1) for financial support.

Funding note Open Access funding enabled and organized by Projekt DEAL.

Conflict of interest The authors declare no conflict of interest.

Supporting information The supporting information is available online at chem.scichina.com and link.springer.com/journal/11426. The supporting materials are published as submitted, without typesetting or editing. The responsibility for scientific accuracy and content remains entirely with the authors. The research data underpinning this publication can be accessed at https://doi.org/10.17630/e89b2529-b213-4a5f-9102-5ed7a2a30ebc

1 Sun D, Si C, Wang T, Zysman-Colman E. *Adv Photon Res*, 2022, 3: 2200203
2 Zou SJ, Shen Y, Xie FM, Chen JD, Li YQ, Tang JX. *Mater Chem Front*, 2020, 4: 788–820
3 Huang T, Jiang W, Duan L. *J Mater Chem C*, 2018, 6: 5577–5596
4 Wong MY, Zysman-Colman E. *Adv Mater*, 2017, 29: 1605444
5 Uoyama H, Goushi K, Shizu K, Nomura H, Adachi C. *Nature*, 2012, 492: 234–238
6 Thejo Kalyani N, Dhoble SJ. *Renew Sustain Energy Rev*, 2012, 16: 2696–2723
7 Wang S, Zhang H, Zhang B, Xie Z, Wong WY. *Mater Sci Eng-R-Rep*, 2020, 140: 100547
8 Xie Y, Li Z. *J Polym Sci Part A-Polym Chem*, 2017, 55: 575–584
9 Sun D, Duda E, Fan X, Saxena R, Zhang M, Bagnich S, Zhang X, Köhler A, Zysman-Colman E. *Adv Mater*, 2022, 34: 2110344
10 Sun D, Saxena R, Fan X, Athanasopoulos S, Duda E, Zhang M, Bagnich S, Zhang X, Zysman-Colman E, Köhler A. *Adv Sci*, 2022, 9: 2201470
11 Abd-El-Aziz AS, Abdelghani AA, Wagner BD, Bissessur R. *Macromol Rapid Commun*, 2019, 40: 1800711
12 Albrecht K, Matsuoka K, Fujita K, Yamamoto K. *Angew Chem Int Ed*, 2015, 54: 5677–5682
13 Burn PL, Lo SC, Samuel IDW. *Adv Mater*, 2007, 19: 1675–1688
14 Zhao G, Liu D, Wang P, Huang X, Chen H, Zhang Y, Zhang D, Jiang W, Sun Y, Duan L. *Angew Chem Int Ed*, 2022, 61: e202212861
15 Zeng S, Xiao C, Zhou J, Dong Q, Li Q, Lim J, Ma H, Lee JY, Zhu W, Wang Y. *Adv Funct Mater*, 2022, 32: 2113183
16 Liu J, Chen L, Wang X, Yang Q, Zhao L, Tong C, Wang S, Shao S, Wang L. *Macromol Rapid Commun*, 2022, 43: 2200079
17 Kim YH, Wolf C, Cho H, Jeong SH, Lee TW. *Adv Mater*, 2016, 28: 734–741
18 Wada Y, Kubo S, Kaji H. *Adv Mater*, 2018, 30: 1705641
19 Wilson JS, Chawdhury N, Al-Mandhary MRA, Younus M, Khan MS, Raithby PR, Köhler A, Friend RH. *J Am Chem Soc*, 2001, 123: 9412–9417
20 Caspar JV, Kober EM, Sullivan BP, Meyer TJ. *J Am Chem Soc*, 1982, 104: 630–632
21 Yu Y, Hu Y, Yang S, Luo W, Yuan Y, Peng C, Liu J, Khan A, Jiang Z, Liao L. *Angew Chem Int Ed*, 2020, 59: 21578–21584
22 Li X, Wang K, Shi YZ, Zhang M, Dai GL, Liu W, Zheng CJ, Ou XM, Zhang XH. *J Mater Chem C*, 2018, 6: 9152–9157
23 Zhang Y, Wu J, Song J, Chen Z, He J, Wang X, Liu H, Chen S, Qu J, Wong W. *Adv Elect Mater*, 2019, 5: 1800677
24 Wang B, Yang H, Zhang Y, Xie G, Ran H, Wang T, Fu Q, Ren Y, Sun

N, Zhao G, Hu JY, Wang Q. *J Mater Chem C*, 2019, 7: 12321–12327
25 Zeng W, Zhou T, Ning W, Zhong C, He J, Gong S, Xie G, Yang C. *Adv Mater*, 2019, 31: 1901404
26 Chen J, Xiao Y, Wang K, Sun D, Fan X, Zhang X, Zhang M, Shi Y, Yu J, Geng F, Lee C, Zhang X. *Angew Chem Int Ed*, 2021, 60: 2478–2484
27 Sharma S, Pal AK. *J Mater Chem C*, 2022, 10: 15681–15707
28 Kim JH, Yun JH, Lee JY. *Adv Opt Mater*, 2018, 6: 1800255
29 Adamo C, Barone V. *J Chem Phys*, 1999, 110: 6158–6170
30 Petersson GA, Tensfeldt TG, Montgomery J. *J Chem Phys*, 1991, 94: 6091–6101
31 Kerwin SM. *J Am Chem Soc*, 2010, 132: 2466–2467
32 Hirata S, Head-Gordon M. *Chem Phys Lett*, 1999, 314: 291–299
33 Connelly NG, Geiger WE. *Chem Rev*, 1996, 96: 877–910
34 Duda E, Hall D, Bagnich S, Carpenter-Warren CL, Saxena R, Wong MY, Cordes DB, Slawin AMZ, Beljonne D, Olivier Y, Zysman-Colman E, Köhler A. *J Phys Chem B*, 2022, 126: 552–562
35 Englman R, Jortner J. *Mol Phys*, 1970, 18: 145–164
36 Xue J, Liang Q, Wang R, Hou J, Li W, Peng Q, Shuai Z, Qiao J. *Adv Mater*, 2019, 31: 1808242
37 Wu L, Huang C, Emery BP, Sedgwick AC, Bull SD, He XP, Tian H, Yoon J, Sessler JL, James TD. *Chem Soc Rev*, 2020, 49: 5110–5139
38 Liu Y, Chen Y, Li H, Wang S, Wu X, Tong H, Wang L. *ACS Appl Mater Interfaces*, 2020, 12: 30652–30658
39 Xie FM, Li HZ, Dai GL, Li YQ, Cheng T, Xie M, Tang JX, Zhao X. *ACS Appl Mater Interfaces*, 2019, 11: 26144–26151
40 Zeng X, Zhou J, Zou S, Tang Y, Li H, He Y, Li Y, Wang W, Tang J. *Adv Opt Mater*, 2022, 10: 2200277
41 Chan CY, Tanaka M, Lee YT, Wong YW, Nakanotani H, Hatakeyama T, Adachi C. *Nat Photon*, 2021, 15: 203–207
42 Sun JW, Lee JH, Moon CK, Kim KH, Shin H, Kim JJ. *Adv Mater*, 2014, 26: 5684–5688
43 Wu S, Kumar Gupta A, Yoshida K, Gong J, Hall D, Cordes DB, Slawin AMZ, Samuel IDW, Zysman-Colman E. *Angew Chem Int Ed*, 2022, 61: e202213697
44 Kim HS, Park SR, Suh MC. *J Phys Chem C*, 2017, 121: 13986–13997
45 Chen D, Cai X, Li XL, He Z, Cai C, Chen D, Su SJ. *J Mater Chem C*, 2017, 5: 5223–5231
46 Woo JY, Park MH, Jeong SH, Kim YH, Kim B, Lee TW, Han TH. *Adv Mater*, 2023, 35: 2207454
47 Murawski C, Leo K, Gather MC. *Adv Mater*, 2013, 25: 6801–6827
48 Oda S, Kawakami B, Yamasaki Y, Matsumoto R, Yoshioka M, Fukushima D, Nakatsuka S, Hatakeyama T. *J Am Chem Soc*, 2022, 144: 106–112
49 Hasan M, Saggar S, Shukla A, Bencheikh F, Sobus J, McGregor SKM, Adachi C, Lo SC, Namdas EB. *Nat Commun*, 2022, 13: 254